N94-21645

9. Earth Observing Scanning Polarimeter

Larry Travis, NASA Goddard Institute for Space Studies

Climate forcing by tropospheric aerosols, discussed briefly above (Section 3), is receiving increased attention because of the realization that the climate effects may be large, while our knowledge of global aerosol characteristics and temporal changes is very poor. Tropospheric aerosols cause a direct radiative forcing due simply to their scattering and absorption of solar radiation, as well as an indirect effect as cloud condensation nuclei which can modify the shortwave reflectivity of clouds. Sulfate aerosols tend to increase planetary albedo through both the direct and indirect effects; Charlson *et al.* (1992) estimate a cooling due to anthropogenic sulfate aerosols of order 1 W/m^2, noting that this is similar in magnitude to the present anthropogenic greenhouse gas warming. Other aerosols, including those from biomass burning (Penner *et al.*, 1992) and wind-blown desert dust (Tanre *et al.*, 1988; Joseph, 1984; Coakley and Cess, 1985) are also of potential climatic importance.

At present, the only global monitoring of tropospheric aerosols is a NOAA operational product, aerosol optical thickness, obtained using channel-1 (0.58-0.68 μm) radiances from the AVHRR (Rao *et al.*, 1988). With this single channel radiance data, one must use an approach which is based on the inferred excess of reflected radiance owing to scattering by the aerosols over that expected from theoretical calculations. This approach is suited only for situations where the surface has a low albedo that is well known *a priori*. Thus, the NOAA operational product is restricted to coverage over the ocean at AVHRR scan angles well away from sun glint, and aerosol changes are subject to confusion with changes caused by either optically thin or subpixel clouds. Because optically thin aerosols have only a small effect on the radiance, accurate measurements for optical thickness less than 0.1 (which is a typical background level) are precluded. Moreover, some of the largest and most important aerosol changes are expected over land.

TABLE 9.1. **EOSP measurement objectives, instrument characteristics and key advantages.**

Measurement Objectives

Global distribution and nature of tropospheric aerosols: optical thickness, particle size and refractive index

Global cloud climatology: optical thickness, cloud-top pressure, particle size, particle liquid/ice phase

Global surface reflectance and polarization

Measurement precision needed to determine interannual and decadal changes of these parameters

Instrument Characteristics

Scans limb to limb perpendicular to or along satellite ground track

Instantaneous field of view of 8 km (at nadir) with 180 samples per scan

Simultaneous radiance and polarization data for 12 bands between 410 and 2250 nm

High precision in-flight calibration with proven long-term stability

Polarization accuracy: 0.2% absolute; precision better than 0.1%

Radiometric accuracy: 5% absolute; decadal precision better than 2%

Key Advantages

High sensitivity to aerosol properties, unattainable with only radiance measurements

Cloud properties more precise than obtainable with existing and planned meteorological satellites; includes detection and measurement of thin clouds, e.g., sub-visible cirrus; high sensitivity to cloud particle shape

Surface reflectance monitored to precision required to quantify decadal change

---

TABLE 9.2. **EOSP predecessor instruments.**

Instrument (Spacecraft)	Operation Period	Spectral Bands	Mass
IPP (Pioneer 10)	Mar 1972 - present	0.45, 0.66 μm	4 kg
IPP (Pioneer 11)	Apr 1973 - present	0.45, 0.66 μm	4 kg
OCPP (Pioneer Venus)	May 1978 - Dec 1992	0.27, 0.37, 0.55, 0.94 μm	5 kg
PPR (Galilieo)	Oct 1989 - present	0.41, 0.68, 0.94 μm	6 kg

Remote sensing of aerosols on other planets is more advanced than for the Earth, because the planetary measurements have made use of the significant additional information contained in the polarization of reflected sunlight. The effectiveness of polarimetry as a remote sensing tool was first convincingly demonstrated by analyses of ground-based observations of Venus (Hansen and Arking, 1971; Hansen and Hovenier, 1974), which were able to deduce basic microphysical and optical properties of the Venus clouds. Since then, spacecraft observations from polarimeters on the Pioneer 10 and 11 missions have provided information about aerosols on Jupiter (Smith and Tomasko, 1984), Saturn (Tomasko and Doose, 1984), and Titan (Tomasko and Smith, 1982) and on Venus from the Pioneer Venus Orbiter mission (Kawabata *et al.*, 1980).

The Earth Observing Scanning Polarimeter (EOSP) instrument, based upon design heritage and analysis techniques developed for planetary missions, will retrieve tropospheric aerosol characteristics from measurements of multispectral radiance and polarization. Moreover, the same radiance and polarization measurements will also provide very precise information on cloud properties and maps of surface characteristics for cloud-free regions. These capabilities also give EOSP the unique ability to discriminate aerosol from clouds and surface. Table 9.1 summarizes the EOSP objectives, characteristics, and advantages. As indicated in Table 9.2, the EOSP predecessor polarimeters on several planetary missions have demonstrated impressive lifetimes (OCPP operations ended after more than 14 years when the spacecraft entered the Venus atmosphere).

EOSP is designed to scan its 12-mrad IFOV from limb to limb through nadir, acquiring approximately 180 measurements of radiance and polarization in each of 12 spectral bands over each scan. The instrument may be oriented on the spacecraft so that it either scans perpendicular to the satellite ground track, thus obtaining global maps at about 10 km resolution (8 km IFOV footprint at nadir), or scans along the ground track, thus providing the capability of viewing a given location from a continuous range of zenith and phase angles as the spacecraft passes overhead. The EOSP on the inclined orbit Climsat spacecraft will employ cross-track scanning, while the polar-orbiting spacecraft will employ along-track scanning. Thus the polar-orbiter will provide rapid scattering angle variation for a given region, optimizing information on aerosol characteristics, while the inclined orbiter provides daily (nearly) global coverage.

The approximate locations of the 12 EOSP spectral bands are illustrated in Fig. 9.1, along with a schematic solar spectrum for reference. These bands cover a wavelength range of a factor of six, which pro-
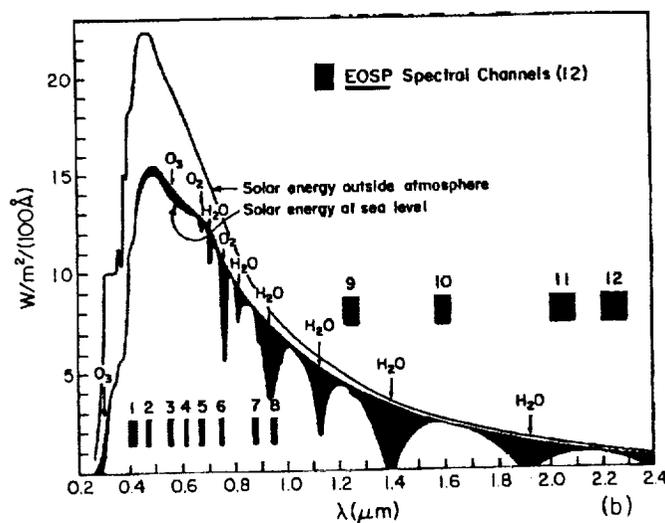
Fig. 9.1. EOSP spectral channels.

vides tremendous leverage for inference of aerosol and cloud particle physical properties (Hansen and Travis, 1974; Coffeen and Hansen, 1972). It is expected that the exact locations of the 12 EOSP bands would be specified during phase B instrument definition, after full science teams are selected for EOSP and Climsat. Bands 1 and 8 (Fig. 9.1) are chosen to be near the extremes of the photodiode detector used for short wavelengths, and a second ultraviolet band (band 2) is located for the purpose of measuring cloud and aerosol altitude from the amount of Rayleigh scattering. The locations of the other five short wavelength bands (3 through 7) still could be adjusted. Similarly, the approximate locations of bands 9 and 12 are chosen to be near the extremes of the infrared detector, but bands 10 and 11 could be adjusted. Because of the high long-term precision of EOSP radiances, if bands are selected appropriately, the results may have a secondary benefit by providing a useful monitoring of surface, vegetation and ocean color properties on decadal time scales, in addition to the basic aerosol and cloud objectives.

The potential for aerosol retrieval is illustrated in Fig. 9.2, which summarizes the analysis of ground-based polarimetry of Venus. Observations at three different wavelengths show how multispectral coverage can be exploited to provide separate sensitivity to various characteristics. At 0.365 μm (panel A), the relatively high contribution from Rayleigh (gas) scattering at middle phase angles provides an 'optical barometer', showing that the cloud tops are at a pressure level of about 50 mb. In panel B, we see that polarization at 0.55 μm was able to constrain particle size with a sensitivity that probably excels that obtainable with many in situ particle size spectrometers. For Venus, the polarimetry at near-infrared wavelengths (panel C) provided a precise determination of the aerosol refractive index, which was the key information identifying the clouds as sulfuric acid.

Retrieval of aerosol properties from planetary polarimetry such as that illustrated in Fig. 9.2 has always employed trial-and-error fitting of the observations by multiple scattering computations for various cloud-aerosol models. Trial-and-error modeling is inappropriate for the routine generation of climate monitoring data products from EOSP. Instead, because of the complex behavior of the polarization, the inversion algorithms will be based on comparing observations with a large number of pre-computed models with parameter ranges spanning those from in situ aerosol measurements. Implementation will entail a decision tree process with tests based on appropriately developed thresholds, ratios, and differences for the multispectral radiance and polarization. With this table look-up approach, the computational requirements for operational processing will be modest; use of large database searches also exploits the very large memory and fast data storage properties of modern computers. The algorithm development and table generation computational effort are well within even present facility resources.
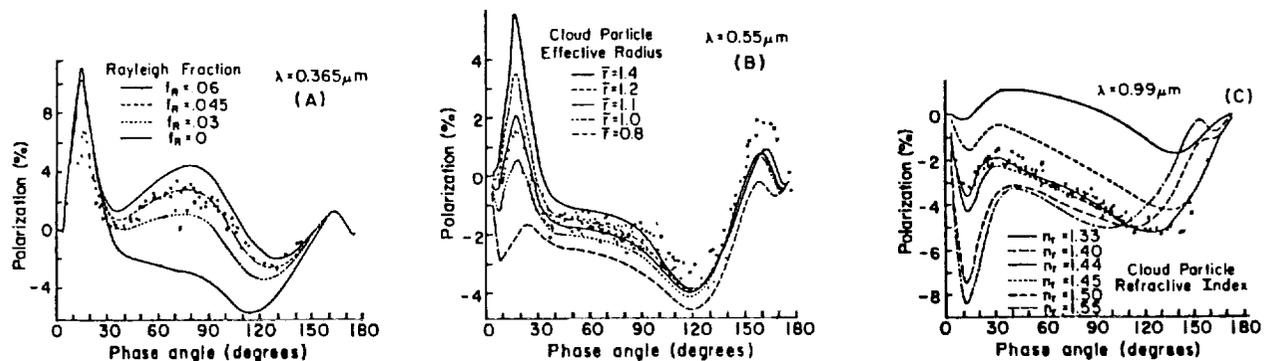
Fig. 9.2. Ground-based polarization studies of Venus clouds.

Aerosol retrieval must distinguish the relative contributions of the atmosphere and the surface. Over the ocean, the surface reflectivity is low (except in the sun glint region) and relatively predictable, so difficulties in extracting aerosol and cloud properties owing to the contribution of the surface to the observed radiance and polarization are minimized. The more interesting and challenging case is over land, where the surface reflectivity and polarization characteristics may be quite variable and are not well known *a priori*. Field measurements of the polarization of the scattered sunlight from vegetation indicate that, to first order, the polarized component arises from light specularly reflected at the leaf surface (Vanderbilt *et al.*, 1985). Because the specular reflection can be determined from the Fresnel equations, given the refractive index of the leaf, a simulation of the expected surface reflectivity and polarization for vegetation is possible since typical spectral properties of plants are adequately known. Such a simulation can demonstrate the ability of EOSP observations to discriminate aerosol and surface effects.

Simulation of the radiance and polarization for sunlight scattered by aerosols is straight-forward using results from many in situ sampling and ground-based remote sensing studies to provide typical ranges of specific aerosol properties. The dominant aerosol component from the perspective of radiative influence globally is the sulfate aerosol generated over land from both natural and anthropogenic SO_2 emissions over land and dimethylsulphide emission from phytoplankton in the ocean (Charlson *et al.*, 1991). The mean particle size for this sulfate aerosol component is typically of order 0.1 to 0.3 μm, and these particles are often more than 50 percent H_2O at the relative humidities typical of the lower troposphere. Larger sized aerosol components are usually due to windblown dust and sea salt. Another aerosol component of increasing importance is smoke from biomass burning, whose typical size distribution is similar to that of the sulfate aerosol (Penner *et al.*, 1992). With the exception of dust, the major tropospheric aerosol components are hygroscopic, so these particles are liquid solutions and hence spherical. As a consequence, Mie scattering computations using the particle optical properties appropriate for the particular aerosol source provide an accurate specification of the single scattering characteristics for the aerosol. As for the irregularly shaped dust particles, there are now techniques (cf., Mishchenko, 1991a,b) which can treat scattering for non-spherical particles without resorting to modified Mie scattering approximations.
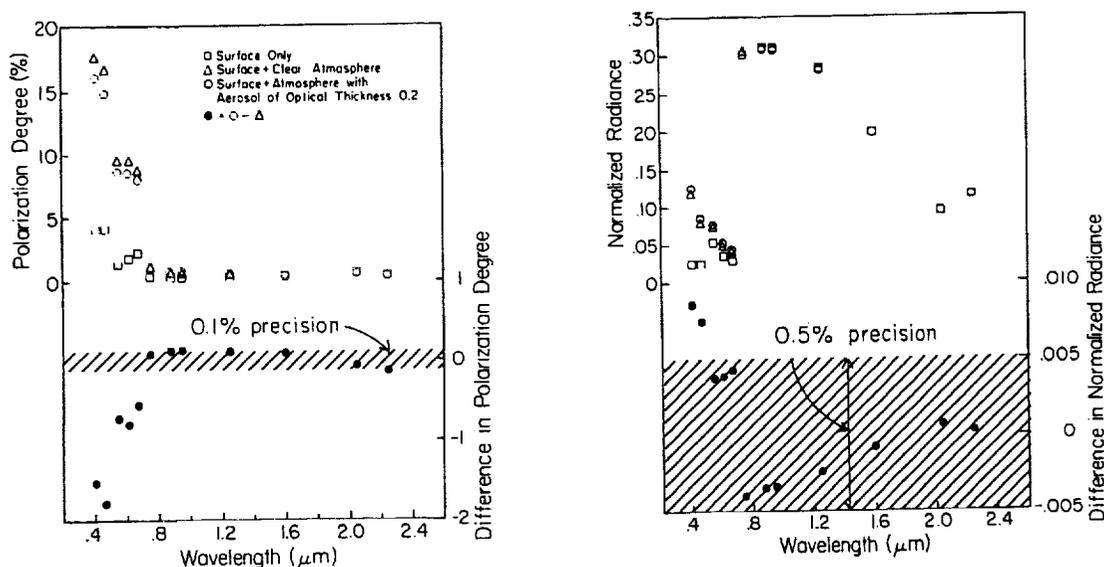
Fig. 9.3. Simulated polarization (left panel) and normalized radiance (right panel) for aerosol of optical thickness 0.2 over a land-vegetation surface. The cumulative contributions of surface, atmosphere (Rayleigh scattering) and aerosol are indicated by the open squares, triangles and circles, respectively for each EOSP spectral band. Filled circles in the bottom portion of each panel show the differences in polarization and normalized radiance between the aerosol and clear atmosphere cases.
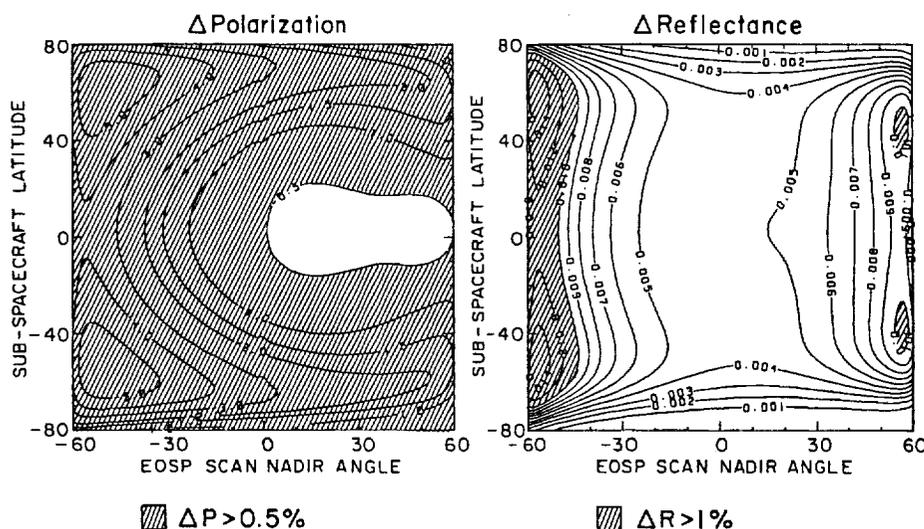
Fig. 9.4. Difference in the polarization and reflectance between clear atmosphere and added aerosol of optical thickness 0.1 for the full range of viewing geometries.

We simulate EOSP data for a vegetation-covered surface by using representative leaf refractive indices (Jacquemoud and Baret, 1990) and assuming that all diffuse leaf scattering (multiple scattering among leaves) is unpolarized (Vanderbilt *et al.*, 1985). For the tropospheric aerosol, we adopt aerosol properties corresponding to the continental model of WCP-55 (1983), viz., a sulfate component of log-normal distribution with geometric mean radius r=0.15 μm and size distribution width σ=1.5, and a dust component with r=0.5 μm, σ=2.5, with number density 0.003 that of the sulfate component. The effective radius (Hansen and Travis, 1974) for the aerosol mixture is r_{eff} = 0.62 μm and the effective variance of the size distribution is v_{eff} = 0.30. Simulations for each of the twelve EOSP spectral bands are made for this aerosol for an optical thickness of 0.2 at 550 nm. The aerosol is distributed through the 300-mb layer just above the vegetation surface, and Rayleigh scattering by the atmosphere is included in the multiple scattering computations.

The simulated polarization for a 15° nadir angle and sub-spacecraft latitude of 36°N (phase angle 38°) is shown in Fig. 9.3a (open circles) and compared with the polarization for the surface alone (squares) and the surface plus clear atmosphere (triangles). Rayleigh scattering dominates the polarization at the shorter wavelengths, with the aerosol causing partial depolarization compared to the clear atmosphere result. This difference is displayed (filled circles) in the lower panel of the figure with an expanded scale. Since the EOSP measurement accuracy for polarization is 0.2%, the depolarization caused by the aerosol at short wavelengths is easy to detect. At the longest wavelengths, the observed polarization is essentially that due to the surface, because of the decreasing scattering efficiency of the aerosols with increasing wavelength. Thus, the wavelength coverage allows easy separation of surface and aerosol polarization effects.

The simulated radiance is shown in Fig. 9.3b, for the same case as the polarization in Fig. 9.3a. As was true for the polarization, Rayleigh scattering dominates over surface reflection at the shortest wavelengths. However, the radiance is much less sensitive than the polarization to the addition of aerosols. Indeed, the optical depth 0.2 appears to be near the limit that can be measured over any surface using only the radiance. That conclusion is consistent with empirical results obtained using AVHRR measurements (Rao *et al.*, 1988).

A further illustration of the greater sensitivity of the polarization than radiance to aerosols is given in Fig. 9.4, which shows the change of polarization and radiance caused by an increase of aerosol optical depth 0.1 for the complete range of observing geometries at the single wavelength 410 nm. Since the *absolute* polarization error is less than 0.2%, any regime with a polarization change greater than 0.5% would have a substantial signal to noise ratio. A comparable signal to noise ratio

for the reflectance can at best be obtained only for extreme nadir viewing angles.

The aerosol size can also be retrieved from the spectral variation of the polarization, and with much less precision from the spectral variation of the radiance. Because the typical aerosol sizes are 0.1-1 μm, there is a strong wavelength dependence of scattering efficiency, and hence optical thickness, throughout the visible and near infrared regions. Aerosols larger than those used for Figs. 9.3 and 9.4 maintain a measurable impact on polarization at longer wavelengths. Any aerosol distribution is also easily distinguished from optically thin or subpixel clouds: cloud opacity is relatively independent of wavelength over the EOSP wavelength range, while the aerosol opacity becomes negligible in the near infrared region.

As has been demonstrated with the studies using Venus polarimetry, the aerosol refractive index can also be deduced from polarization measurements. Those analyses have relied on being able to look at the same region from a range of scattering angles, or equivalently, a situation in which the aerosol structure and characteristics are uniform over a large horizontal extent. Accordingly, the scanning strategy proposed entails obtaining such multiple scattering angle coverage with along-track scanning on the polar, sun-synchronous Climsat spacecraft, while using cross-track scanning on the inclined orbit spacecraft to provide daily global mapping.

Fig. 9.5. Simulated polarization over an EOSP scan at the 410 nm band for a uniform cloud of optical thickness 10 and a cloudtop pressure of 500 mb (top panel). Differences in the polarization for 200, 300, and 400 mb cloudtop pressures compared to the 500 mb case are displayed in the bottom panel.

Accurate cloud properties can be obtained from polarimetry as demonstrated by observations of other planets, simulations for terrestrial clouds, and near-infrared aircraft measurements (Coffeen and Hansen, 1974). Cloud-top height and total cloud optical thickness are primary cloud parameter objectives because of their first-order importance in describing the radiative effects of the cloud. Because of the great difference in polarization of light scattered by air molecules (Rayleigh scattering) and cloud particles, the degree of polarization in the ultraviolet region provides a simple measure of cloud top pressure. Figure 9.5 is a simulation for the 410 nm EOSP band, showing the varying effect of Rayleigh scattering for different cloud top pressures. The top panel is the polarization as a function of scan element for a uniform cloud of 10 μm radius water droplets, with the cloud optical thickness 10 and the cloud top pressure 500 mb. The polarization peak at phase angle near 40° is the rainbow feature, while the strong increase for phase angles greater than about 70° is due entirely to Rayleigh scattering. Since the Rayleigh scattering optical thickness is proportional to the amount of atmosphere above the cloud, the increase of polarization at moderate phase angles varies with cloud top pressure. This is illustrated in the lower panel of Fig. 9.5, which shows the change in polarization caused by moving the cloud top from 500 mb to 400, 300 and 200 mb.

Cloud remote sensing algorithms have relied on the higher visible radiance levels of thicker clouds for generating an estimate of cloud optical depth (Rossow et al., 1989). However, such an approach is often subject to ambiguity, especially for smaller optical thicknesses and small cloud
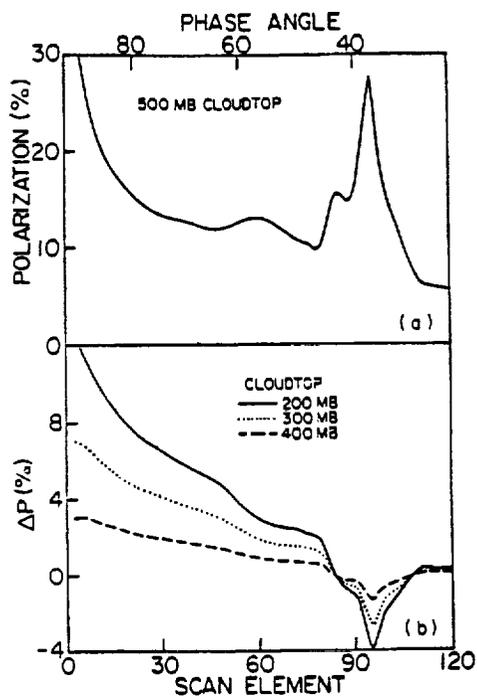
particle sizes. Moreover finite resolution of
satellite measurements can lead to some radiance
variability associated with partial coverage of
the IFOV by clouds. Observations at near-
infrared wavelengths, where water absorption is
important, are potentially sensitive indicators of
cloud particle size and optical depth (Hansen
and Pollack, 1970); these indicators are not too
sensitive to partial cloud cover effects (Han,
1992) Accordingly, techniques based upon
multispectral radiances, including especially
near-infrared bands, are being advanced
(Nakajima and King, 1990; Han, 1992). Even
greater sensitivity to cloud properties is
provided by polarimetry. Polarization is usually
more sensitive to cloud microstructure than is
the intensity (Coffeen and Hansen, 1974); thus
polarization measurements are particularly use-
ful in detecting and characterizing optically thin
clouds, which pose significant difficulties for

TABLE 9.3. **EOSP data product accuracies.**

	Single Field of View	Monthly 500 km Mean
Aerosols		
Optical Thickness	0.03	0.01-0.02
Particle Size	25%	10%
Refractive Index	0.05	0.02
Clouds		
Optical Thickness	10%	5%
Cloud-top Pressure	30 mb	15 mb
Particle Size	25%	10%
Surface		
Reflectance	0.02	0.01
Polarization	0.5%	0.3%

algorithms employing intensity alone. Use of EOSP and MINT observations together allows for direct
determination of partial cloud cover in the IFOV by measuring the relative contributions of Rayleigh
and Mie scattering. With new advances in treatment of scattering by non-spherical particles,
information about ice cloud particles may also be attainable from EOSP measurements.

Table 9.3 summarizes the estimated accuracies for the aerosol, cloud, and surface properties
that EOSP will monitor. The uncertainties in a single 'pixel' retrieval can be substantially reduced
by averaging the results over time and spatial scales of relevance to climate, such as monthly means
at 500 km resolution. These EOSP accuracies are generally much higher than possible with current
satellite instruments, such as the operational AVHRR instruments used for ISCCP analyses. For some
quantities, such as cloud height, the Michelson Interferometer is capable of providing higher
accuracy. We also note that recent experience with AVHRR data (Han, 1992) suggests that the
precision of variations of cloud particle size and optical thickness from place to place and time to time
can be much higher than the estimated absolute accuracy. Thus, because of the much better
calibration and stability of EOSP compared to AVHRR the precision of the measured changes may
be significantly better than our estimates. A summary of our error estimates for all the parameters,
and a comparison with the requirements, is given in Table 7.4.